ACS Photonics

Article

pubs.acs.org/journal/apchd5

Collective Plasmonic Properties in Few-Layer Gold Nanorod Supercrystals

Cyrille Hamon,[†,‡] Sergey M. Novikov,[†,‡,§] Leonardo Scarabelli,[†] Diego M. Solís,[∥] Thomas Altantzis,[⊥] Sara Bals,[⊥] José M. Taboada,[#] Fernando Obelleiro,[∥] and Luis M. Liz-Marzán*[,†,○]

[†]Bionanoplasmonics Laboratory, CIC biomaGUNE, Paseo de Miramón 182, 20009 Donostia - San Sebastián, Spain

[∥]Department Teoría de la Señal y Comunicaciones, University of Vigo, 36301 Vigo, Spain

[⊥]EMAT-University of Antwerp, Groenenborgerlaan 171, B-2020 Antwerp, Belgium

[#]Department Tec. Computadoras y Comunicaciones, University of Extremadura, 10003 Cáceres, Spain

[○]Ikerbasque, Basque Foundation for Science, 48013 Bilbao, Spain

Supporting Information

ABSTRACT: Gold nanorod supercrystals have been widely employed for the detection of relevant bioanalytes with detection limits ranging from nano- to picomolar levels, confirming the promising nature of these structures for biosensing. Even though a relationship between the height of the supercrystal (i.e., the number of stacked nanorod layers) and the enhancement factor has been proposed, no systematic study has been reported. In order to tackle this problem, we prepared gold nanorod supercrystals with varying numbers of stacked layers and analyzed them extensively by atomic force microscopy, electron microscopy and surface enhanced Raman scattering. The experimental results were compared to numerical simulations performed on real-size supercrystals composed of thousands of nanorod building blocks. Analysis of the hot spot distribution in the simulated supercrystals showed the presence of standing waves that were distributed at different depths, depending on the number of layers in each supercrystal. On the basis of these theoretical results, we interpreted the experimental data in terms of analyte penetration into the topmost layer only, which indicates that diffusion to the interior of the supercrystals would be crucial if the complete field enhancement produced by the stacked nanorods is to be exploited. We propose that our conclusions will be of high relevance in the design of next generation plasmonic devices.

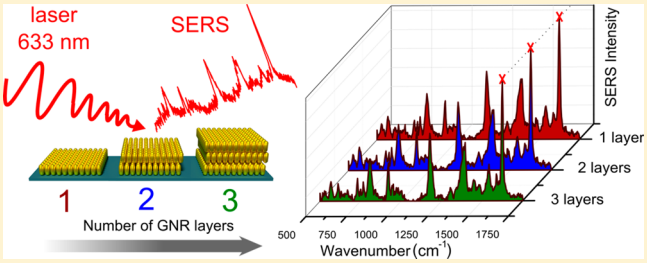

KEYWORDS: *gold nanorods, supercrystal, superlattice, method of moments, MLFMA, SERS, surface enhanced Raman scattering, electron tomography*

Gold nanoparticles display exciting optical properties in the visible and near-IR spectral regions due to localized surface plasmon resonances that can be precisely tuned through variations in particle shape and size.[1−4] Additionally, the organization of gold nanoparticles into ensembles leads to the emergence of new plasmon resonances unattainable by the individual particles, and the resulting optical properties can be further tuned and even amplified.[5−8] Gold nanorods (GNR) are one of the most relevant shapes due to the ease of synthesis, the possibility to form highly organized structures trough directed self-assembly and tunability of the optical properties across a broad spectral range by aspect ratio variation.[2,9−11] Therefore, supercrystal structures made of GNR find a broad interest in fields ranging from sensor design to catalysis and light harvesting systems and are particularly interesting in plasmon enhanced spectroscopy.[12−18] In particular, surface enhanced Raman scattering (SERS) is a vibrational spectroscopy technique furnishing chemical fingerprint-like information on a substance of interest, which can be detected with a high sensitivity at the surface of plasmonic nanostructures.[19,20] The enhancement of the otherwise extremely weak Raman signal requires strong electromagnetic fields in the vicinity of the analyte and these conditions are achieved at the surface of plasmonic nanostructures. Such strong electric fields at plasmonic surfaces can be achieved by inducing coupling of plasmon modes between closely spaced nanoparticles, creating so-called "hotspots".[5,6,12,21,22]

Previous studies showed that among all possible GNR packing and orientations, 3D colloidal crystals (i.e., supercrystals) are one of the most promising architectures for enhancing Raman scattering.[23−25] Indeed, the intralamellar hexagonal order maximizes the number and density of the formed hotspots and their homogeneous distribution permits more reproducible and quantitative SERS measurements. During the last five years, several research groups reported the detection of relevant bioanalytes using GNR supercrystals as SERS substrates, with a detection limit ranging from

Received: July 5, 2015
Published: September 3, 2015

DOI: 10.1021/acsphotonics.5b00369
ACS Photonics 2015, 2, 1482−1488

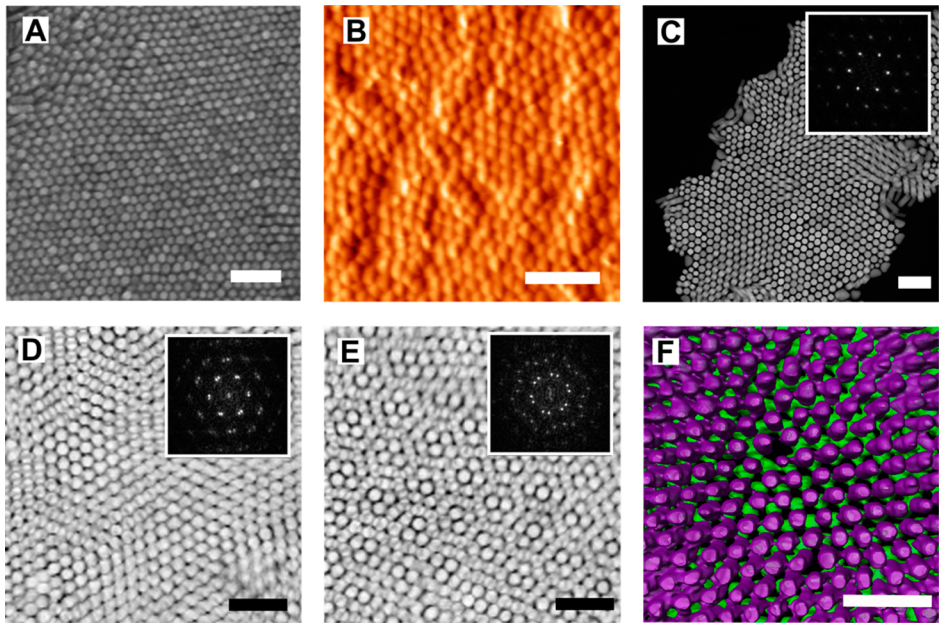

Figure 1. Characterization of the GNR organization within supercrystals. (A) SEM image of the top surface of a supercrystal. (B) AFM image of a supercrystal surface. (C–E) HAADF-STEM images of different supercrystals, standing on a SiN film, including a monolayer (C) and two different bilayers (D, E). Insets are FFT of the image. Moiré patterns result from a small angular misorientation between neighboring GNR sheets that can be determined from the corresponding FFT. (F) Electron tomography reconstruction image of a GNR bilayer showing the top layer in purple and the bottom layer in green. All scale bars are 100 nm.

nanomolar to picomolar concentrations, which confirms the suitability of these structures toward biosensing.[24,26,27] For example, Xion et al. demonstrated femtomolar detection of food contaminants on a GNR monolayer.[26] Our group has shown attomolar detection of scrambled prions in blood and serum, supported on micron-scale supercrystals containing a large number of stacked GNR layers.[24] Even though a relationship between the height of the supercrystal (i.e., the number of stacked GNR) and the enhancement factor (EF) of those architectures has been suggested, a systematic study, including detailed simulations, is still lacking. Therefore, a better understanding of such effects is of great interest and would pave the way toward an optimized architecture design.

In the present work, we carried out a careful SERS investigation on supercrystals comprising different numbers of stacked layers. This systematic study relied on the fabrication by drop casting of highly organized GNR assemblies, thanks to a particular amphiphilic alkanethiolate coating.[28−30] Correlated electron and atomic force microscopies, as well as Raman scattering spectroscopy, were used to characterize the organization and optical properties of the supercrystals, respectively. Importantly, the experimental results are supported by an ad hoc implementation of the full-wave numerical method recently introduced in the context of nanoplasmonics,[31] which is based on the surface integral equation-method of moments (MoM) and the multilevel fast multipole algorithm (MLFMA).[31−33] It must be emphasized that rigorous modeling of such large-scale, densely packed nanoparticle arrangements is highly challenging, even when using the most advanced available surface integral equation techniques, let alone solving it with volumetric approaches. We exploited here the repetition pattern, taking into account the periodicity inherent to these structures but without resorting to infinite-structure approximations, which would omit edge effects.[32] Furthermore, the rank-deficient nearest-neighbor couplings of quasi-electrostatic nature due to the deep subwavelength overpopulated surface meshes required in plasmonics are algebraically compressed. Overall, the dramatic reduction in computational cost (regarding both runtime and memory) achieved with this method allowed us to simulate supercrystals composed of tens of thousands of GNR building blocks, thereby allowing us to accurately predict the scattering response from a complex plasmonic system with dimensionally realistic simulation boxes.

RESULT AND DISCUSSION

Gold nanorods (58 ± 5 nm long; 17 ± 2 nm thick) were synthesized according to previously reported protocols (Figure S1).[34,35] Importantly, the as-synthesized GNR were monodisperse in size, resulting in the spontaneous formation of supercrystals upon drying. However, because the morphology and intralamella organization of the supercrystals were difficult to control, the GNR were coated with an amphiphilic alkanethiolate (1-mercaptoundec-11-yl)hexa(ethylene glycol), denoted here as MUDOL (Figures S2 and S3).[28−30] Remarkably, not all GNR were found to orient perpendicular to the substrate, but the obtained supercrystals were found to be rather monodisperse in terms of lateral dimensions, with a quasi-circular shape of about 4 μm in diameter, regardless of the initial GNR concentration used for drop casting (Figures S4 and S5). Within the same casting experiment, a larger number of stacked layers were usually found closer to the edge of the drop, most likely because of the well-known coffee stain effect (Figure S6), and in general supercrystals were obtained containing between 1 and 20 monolayers, depending on initial rod concentration. For example, supercrystals prepared with an initial concentration of $[Au^0]$ = 3 mM displayed between one and five layers inside the coffee ring. The high level of organization of the nanorods and the homogeneous distribu-

DOI: 10.1021/acsphotonics.5b00369
ACS Photonics 2015, 2, 1482−1488

tion of the supercrystal were undoubtedly advantageous toward the realization of this work.

The structure and local organization of the nanorods within the supercrystals was thoroughly investigated, as summarized in Figure 1. The hexagonal intralamellae order of the nanorods was observed by scanning electron microscopy (SEM; Figure 1A), and atomic force microscopy (AFM), high angle annular dark field scanning transmission electron microscopy (HAADF-STEM), and electron tomography (Figure 1B−F) confirmed the SEM observations. AFM images revealed a small degree of roughness at the surface of the supercrystals, which may arise from a slight polydispersity in the length of the GNR or from some roughness in the glass support. In HAADF-STEM, however, the substrate roughness was considerably lower and additionally allowed the precise determination of the separation distances between adjacent nanorods within a single layer, which was found to be 2 nm (Figure 1C). Remarkably, Moiré interference patterns in images of multilayers were observed due to a small degree of rotational offset between two neighboring layers,[36,37] demonstrating the quasi-crystalline symmetry of the GNR multilayer assemblies (Figure 1D,E). The 6-fold symmetry in a hexagonal lattice implies that each 30° rotation is equivalent to a 0° rotation; therefore, the Moiré patterns in Figure 1D,E correspond to a misorientation angle of 8° and 18°, respectively. Three-dimensional characterization of the supercrystals by electron tomography confirmed the misorientation of the GNR layers, as well as ABA-type stacking, which could be used as an input for modeling studies or during the interpretation of optical properties. A movie is also provided in the Supporting Information. The Moiré interference patterns were found to be different from one supercrystal to another, meaning that the misorientation angle between two layers was not always the same (Figure 1D,E). A similar aperiodicity has been reported for semiconductor (CdS) nanorod supercrystals, suggesting a strong similarity in the formation mechanism for semiconductor and gold nanorod supercrystals. Ryan and co-workers explained the formation of CdS nanorod superstructures by a primary assembly of ordered sheets in solution followed by a layer-by-layer process in which each monolayer would randomly settle on top of another, which may well be the case here (discussion on the supercrystal formation mechanism is out of the scope of the present work).[36]

Next, aiming at the study of the optical properties of the GNR supercrystals, dark field microspectroscopy, electron energy loss spectroscopy (EELS), and SERS were conducted. It should be mentioned that the dark field measurements were not conclusive and thus are not represented here. Indeed, it is likely that the nanorods are too close to each other, so that the (multi)layer system would behave as a continuous film in far field. Nonetheless, the optical properties of the supercrystals were described by means of EELS and SERS so as to map the spatial distribution of the plasmon modes and the electric field enhancements, respectively. The EELS experiments were carried out on monolayers and bilayers and hotspots could be clearly identified at the gaps between nanorods. A strong peak for monolayers located around 500−550 nm was noted (Figure S8), whereas three peaks were observed in the case of the bilayer, one around 500−550 nm and two others that were red-shifted toward 690−890 nm (Figure S9). Although interpretation of these results is far from straightforward, a clear difference can be appreciated between the response of monolayers and bilayers, which is likely related to field enhancement distributions as discussed below.

The optical properties of the supercrystals were further investigated through their SERS performance, as shown in Figure 2. Prior to SERS analysis, the substrates were cleaned by

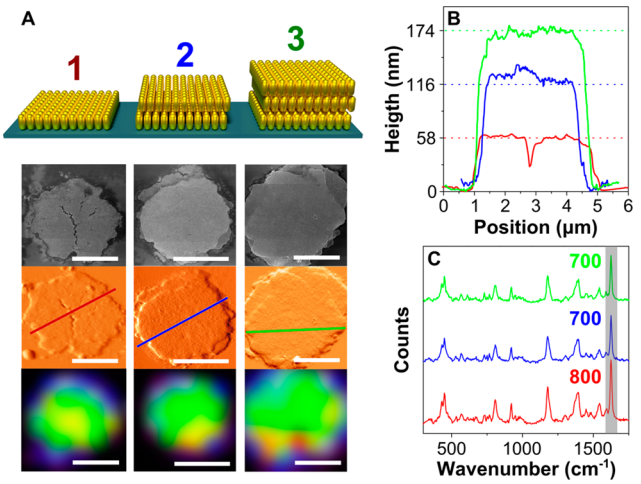

Figure 2. Optical characterization of mono-, bi-, and trilayered GNR supercrystals. (A) Schemes depicting mono-, bi-, and trilayered supercrystals together with (top to bottom): SEM, AFM, and SERRS images. SERRS images were obtained by mapping the SERRS intensity of the crystal violet vibrational peak over 1618−1632 cm^{-1}. Scale bars are 2 μm on all nine images. (B) Height profiles of a monolayer (red), a bilayer (blue), and trilayer (green) along the lines shown on the AFM image in (A); the dotted lines indicate the expected values for mono-, bi-, and trilayers. (C) Average SERRS spectra of crystal violet measured on a monolayer (red), bilayer (blue), and trilayer (green). The shaded gray column indicates the integrated spectral range for generating SERRS images in (A). Concentration of CV solution was 10^{-6} M, acquisition time was 500 ms, and laser power at the sample was ≈0.01 mW, at an excitation wavelength of 633 nm.

Ar^+ plasma treatment to remove organic material deposited on top of the supercrystals, which could interfere with the measurements. Details and comparison between different cleaning procedures are provided in the Supporting Information (Figure S7). Crystal violet (CV) was selected as a model analyte because of its well-known chemical and physical features. After plasma cleaning, CV was drop casted on the supercrystals, and SERS mappings were recorded at various positions of the substrate. CV deposition was considered to be uniform, taking into account the small region of interest, so that all supercrystals were similarly covered by the analyte as required for a meaningful comparison of the SERS intensities. Importantly, the SERS measurements were performed prior to structural characterization, as both the electron beam in SEM and the tip in AFM could eventually charge, contaminate or damage the surface of the supercrystals. This systematic optical and structural characterization was carried out on a large number of supercrystals with different numbers of layers on the same drop casted sample (for each selected number of layers at least 10 different supercrystals were identified and measured). We focused on supercrystals containing up to three layers. Figure 2A shows a schematic representation of the mono-, bi-, and trilayered supercrystals and their systematic characterization by SEM, AFM, and SERS. In particular, height profiles measured in AFM were found to be in agreement with multiple values of the average GNR length, thereby confirming the

DOI: 10.1021/acsphotonics.5b00369
ACS Photonics 2015, 2, 1482−1488

lamellar order within the supercrystals and allowing us to precisely determine the number of layers in each GNR supercrystal. Indeed, heights of 58, 117 and 174 nm were measured precisely corresponding to one, two and three times the average rod length, respectively (Figure 2B). All measurements were performed at an excitation wavelength of 633 nm, which matches the absorption band of CV, meaning that we actually measure surface enhanced resonant Raman scattering (SERRS). SERRS images were acquired by mapping the spatial dependence of SERRS intensity integrated over the shift range of 1618−1632 cm^{-1}, corresponding to the most intense vibrational peak of CV. Remarkably, in all cases the SERRS signal intensity was uniform throughout the entire supercrystal surface and only the chemical fingerprint of CV was detected, with an average maximum intensity of 700 counts (Figure 2C). Note that the intensity of the signal was relatively high taking into account the small integration time (500 ms) and low laser power (0.01 mW) used in this experiment. Another important issue that needs to be considered is the presence of edge effects, which can significantly affect the collection and interpretation of the SERRS data. In this respect it is important to underline that the laser spot size (λ = 633 nm) was around 1 μm in diameter, that is, substantially smaller than the dimensions of the supercrystals. The hexagonal packing of the nanorods was confirmed in all cases on the top layer of the supercrystals (Figure 1). Although small height variations were noted on the supercrystal surface by AFM, these did not impact the measured SERRS signal. On the other hand, anomalously higher intensity spots in the SERRS mapping images corresponded to spherical byproducts or randomly oriented GNR on the supercrystal upper surface (Figure S10), which may lead to the presence of additional plasmon modes. Two important conclusions can be drawn from this analysis: first, SERRS mappings were crucial to assess the homogeneity of the field enhancement within GNR supercrystals, as higher signals are recorded on local defects (i.e., single point measurements are not reliable); second, increasing the number of layers in a GNR supercrystal not necessarily represents a benefit for the SERRS signal in this case. Additional SERS measurements on supercrystals comprising up to nine layers are displayed in the Supporting Information, showing that in all cases the maximum SERRS intensity was uniform at near 700 counts, regardless of the total number of stacking layers (Figures S10−S11). The analytical enhancement factor of these supercrystals was determined to be 1.23×10^7 and was calculated as the ratio between the Raman scattering intensity of CV in the presence and in the absence of GNR supercrystal, using the same experimental parameters.[38]

To better understand the experimental results, we carried out detailed electromagnetic simulations based on MLFMA-MoM to determine the local electric field distribution and SERRS intensity for supercrystals comprising one, two, and three monolayers, but also trying to estimate the effect of additional layers. In the experiments, over 1000 GNRs contribute to the optical excitation in the focal volume of the laser beam. We thus aimed at simulating supercrystals composed of a large number of nanorods, so as to closely describe this complex system. Specifically, 3600 GNR were used for a monolayer (≈3500 in a real system), 7200 GNR for bilayers (≈7000 in a real system), 10800 for trilayers (≈10000 in a real system), and 14400 for tetralayers (≈14000 in a real system). It is important to stress that the number of unknowns in the calculation of the tetralayer case was above 47.6 million, which is far beyond the computational limits that have been reported so far in the literature.[32] Even though modeling of supercrystals with even larger dimensions was possible, it was considered impractical due to the high computational cost (ca. 5 h per wavelength were required for the tetralayer case, on a workstation with four 8-core Intel Xeon E7−4820 processors at 2 GHz). Simulations were carried out considering illumination at normal incidence (parallel to the GNR long axis) and linear polarization in the plane of the substrate. In the simulation, the incident light was focused onto the crystal surface with a numerical aperture of 0.85, in accordance with the experimental setup. In order to simulate the lens effect as real as possible we superposed two incident polarized plane waves impinging from opposite azimuthal directions (ϕ_{inc} and $\phi_{inc} + \pi$), both with the same elevation angle, defined from the numerical aperture (NA = 0.85) as the angle between the wave direction and the normal to the crystal surface, ϕ_{inc} = arcsin(NA). Additionally, the resulting incident field is tapered by a two-dimensional Gaussian window with zero mean and standard deviation $0.15\lambda_{inc}$. In this way we get a simple and realistic model for the incident field, avoiding the use of paraxial approximations. For further similarity with the experimental system, we considered GNR with octagonal cross section and dimensions of 58 nm in length and 17 nm in width, with a fixed distance between rods in the supercrystals of 2 nm, according to previous reports.[28,29,39] We simulated GNR supercrystals having a missorientation angle of 15° between two layers and an ABAB-type interlamellar packing, in an attempt to simulate the real experimental system.

The SERS intensity was simply calculated as $|E\ (633\ nm)|^4$ and was not only determined on the surface of the nanostructures, but also inside, which allowed us to evaluate the hotspot distribution and intensity, as a function of the number of layers (Figure 3). Interestingly, the results indicate that SERS enhancement was essentially the same at the surface of all supercrystals, around 10^4, and was higher at the gaps between nanorods, suggesting that the analyte would need to diffuse into the space between the nanorods if a more sensitive SERS detection were to be achieved (Figure 3). We therefore selected an analyte penetration depth of about 8 nm into the structures, in order to obtain comparable results between simulations and experiments, where we assumed that cleaning of the supercrystal surface by Ar^+ plasma treatment leads to improved penetration of the analyte in the GNR structure. Additionally, the arrangement of the nanorods was observed to originate standing waves, which were distributed at different resonant depths according to the number of layers composing the supercrystals.[31] In this respect, more intense hotspots were distributed at various locations for different supercrystals: maximum hotspot intensity was higher at the bottom side of a monolayer, but higher on the top for a bilayer, at the middle layer for the trilayer and higher at the top layer for the tetralayer case (Figure 3A−D). In general, it could be stated that supercrystals comprising an odd number of layers display maximum enhancement at the inner structure, whereas supercrystals comprising an even number of layers have maximum enhancement at the very top, suggesting a symmetry effect on hotspot localization. The enhancement at the top layer was found to depend on the standing-wave pattern associated with the combination of the incident wave and the wave reflected at the bottom of the crystal. Therefore, this enhancement depends on the total depth of the structure (which in turn depends on the length of the nanorods, the

DOI: 10.1021/acsphotonics.5b00369
ACS Photonics 2015, 2, 1482−1488

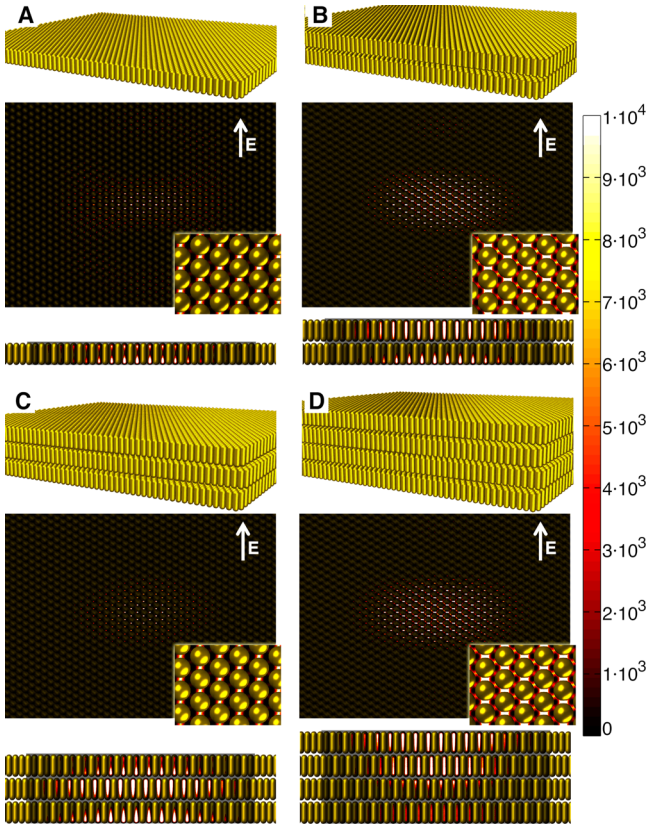

Figure 3. Simulation of hotspot distribution within supercrystals. (A–D) SERS performance (calculated as $|E$ (633 nm)$|^4$) of GNR supercrystals with different number of layers, simulated by MLMFA-MoM. In each case, the hotspot distribution is represented both as top view and cross section: (A) monolayer; (B) bilayer; (C) trilayer; (D) tetralayer. Arrows on top view images indicate in-plane polarization direction.

interlamellae distance, and the number of layers) and the wavelength of the laser that is being used. In our particular case, maximum enhancement occurring at the top layer was found for supercrystals with an odd number of layers but could also appear for an even number, if the above-mentioned parameters were varied. The enhancement versus depth dependence follows a standing-wave pattern that can be clearly observed in the provided movies (S3, S4, S5, S6).

In the simulation, we characterized standing wave patterns that in turn increased the total number of hotspots within the supercrystals as the number of layers was increased, thus, we may expect an increase in the signal of multilayers compared to monolayers. However, this is not in agreement with the experiment, in which all supercrystals yielded similar SERRS intensity, regardless of the number of layers. Again, this is likely to be related to the limited penetration of the analyte (about 8 nm deep in the first layer), as the self-assembled monolayer comprises MUDOL at the GNR surface, and the alkyl chains are likely to interdigitate so as to maintain the close packing, thereby precluding diffusion of the analyte within the structure. It is worth noting that the mismatch between the EF obtained in the experiment (near 10^7) and in the simulation (around 10^5) can be explained by the additional chemical enhancement and due to the resonance matching of CV at 633 nm in the experiment (SERRS vs SERS).

As stated above, we find that the measured SERS signal of an analyte on a GNR supercrystal arises from the upper layer only. We therefore calculated the SERS enhancement at the upper surface of the supercrystals, as a function of the excitation wavelength. In agreement with the experiment, when an excitation wavelength of 633 nm is used, the SERS signal is found to be almost identical for all supercrystals (Figure 4).

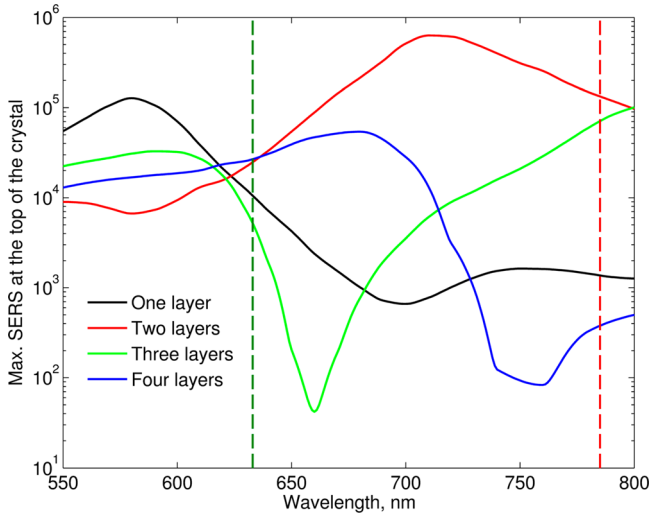

Figure 4. Calculated maximum SERS intensity at the upper surface of a supercrystal, as a function of the excitation wavelength. The dotted lines indicate the excitation wavelengths experimentally used in this work.

Interestingly, in the spectral region considered, a maximum SERS signal at 580 nm was obtained for monolayers whereas for the trilayer the maximum shifted toward the IR region. A maximum was observed for bilayers at 710 nm, which is close to the maximum determined at 680 nm for tetralayer supercrystals. Therefore, the near field simulation confirms that the standing wave pattern strongly depends on the frequency of the incident light. In light of these simulations, we carried out an additional SERS investigation at 785 nm (Figures S12 and S13). A clear trend was observed showing that monolayers lead to 2-fold smaller SERS signal than multilayers, confirming the results of the simulations (Figure 4). It is worth noting that the difference of signal between monolayers and bilayers is less than the predicted 100-fold. It is important to take into account that this near field plot only considers the enhancement factor at a horizontal plane, 8 nm deep in the upper layer, whereas an integration in three dimensions would better describe the system. In our case, this was not attempted because of the high computational cost. Note that small difference between the experiment and the simulation parameters can lead to significant variations in the standing wave pattern even if the model aims at describing as close as possible a GNR supercrystal. Overall, the measured SERS signal was the same for all supercrystals at 633 nm excitation, in good agreement with the simulation, but variations of the signal at 785 nm excitation were found between monolayers and multilayers.

CONCLUSIONS

Robust plasmonic substrates displaying a high level of organization, with orientation of gold nanorods perpendicular to the substrate, were obtained by simple drop casting. The structural and optical properties of such GNR supercrystals were investigated by various microscopy and spectroscopy techniques, with the objective to investigate the relation

DOI: 10.1021/acsphotonics.5b00369
ACS Photonics 2015, 2, 1482–1488

between the number of monolayers in GNR supercrystals and their performance in Raman scattering enhancement. The results showed that the SERS signal on gold nanorod supercrystals is very homogeneous when using an excitation wavelength of 633 nm, regardless of the number of layers, whereas variations can be observed at 785 nm. The experimental results were supported by accurate full-wave electromagnetic simulations using the M^3 solver. This is an ad hoc implementation of MLFMA,[32] yielding a dramatic reduction of the required memory footprint as plasmonic systems up to 47.6 million unknowns were simulated with a very small memory footprint of around ∼2 GB. This high performance computational study predicted the presence of a dense distribution of hotspots at different resonant depths depending on the number of GNR layers. Overall, the results were interpreted by considering a short penetration depth of the analyte between the nanorod gaps, only at the upper layer of all GNR supercrystals. Simulations were additionally used to predict further enhancements at different excitation wavelengths that could not be measured on our experimental setup but open possibilities to further studies. Improvements on supercrystal design allowing analyte diffusion are predicted to yield significantly higher enhancements that could pave the ways for next generation plasmonic devices, not only in sensor design, but also in other fields such as catalysis or light harvesting systems.

■ ASSOCIATED CONTENT

Supporting Information

The Supporting Information is available free of charge on the ACS Publications website at DOI: 10.1021/acsphotonics.5b00369.

Material and method sections, including details on GNR preparation, ligand exchange, details on modeling, TEM images of the GNR and corresponding UV−vis spectra, SEM images of CTAB-GNR supercrystals, SEM images of MUDOL-GNR supercrystals obtained from different [Au^0] concentration, AFM characterization of the supercrystals, optimization of cleaning procedure on the supercrystals, EELS characterization of monolayer and bilayers, additional SERS characterization of multilayers, and comparison of crystal violet SERS spectra on supercrystals at different wavelength (PDF).

A movie showing the three-dimensional rendering of a GNR bilayer obtained by electron tomography (S2).

Four movies demonstrating the enhancement versus depth dependence follows a standing-wave pattern for a monolayer (S3), a bilayer (S4), a trilayer (S5) and a tetralayer (S6).

■ AUTHOR INFORMATION

Corresponding Author

*E-mail: llizmarzan@cicbiomagune.es.

Present Address

§Department of Technology and Innovation, University of Southern Denmark, Odense M, DK-5230 Denmark (S.M.N.).

Author Contributions

‡These authors contributed equally (C.H. and S.M.N.).

Notes

The authors declare no competing financial interest.

■ ACKNOWLEDGMENTS

The authors are thankful to Dr. Luis Yate for assistance with sample preparation. This work was supported by the European Research Council (ERC Advanced Grant #267867 Plasmaquo and ERC Starting Grant #335078 Colouratom) and the Spanish Ministerio de Economía y Competitividad (MAT2013-46101-R). D.M.S., J.M.T., and F.O. acknowledge funding from the European Regional Development Fund (ERDF) and the Spanish Ministerio de Economía y Competitividad (MAT2014-58201-C2-1-R, MAT2014-58201-C2-2-R, Project TACTICA), from the ERDF and the Galician Regional Government under Projects CN2012/279 and CN2012/260 (AtlantTIC) and the Plan I2C (2011−2015), and from the ERDF and the Extremadura Regional Government (Junta de Extremadura Project IB13185).

■ REFERENCES

(1) Burda, C.; Chen, X.; Narayanan, R.; El-Sayed, M. A. Chemistry and Properties of Nanocrystals of Different Shapes. *Chem. Rev.* **2005**, *105*, 1025−1102.

(2) Huang, X.; Neretina, S.; El-Sayed, M. A. Gold Nanorods: From Synthesis and Properties to Biological and Biomedical Applications. *Adv. Mater.* **2009**, *21*, 4880−4910.

(3) Dreaden, E. C.; Alkilany, A. M.; Huang, X.; Murphy, C. J.; El-Sayed, M. A. The Golden Age: Gold Nanoparticles for Biomedicine. *Chem. Soc. Rev.* **2012**, *41*, 2740−2779.

(4) Skrabalak, S. E.; Xia, Y. Pushing Nanocrystal Synthesis toward Nanomanufacturing. *ACS Nano* **2009**, *3*, 10−15.

(5) Jain, P. K.; El-Sayed, M. A. Plasmonic Coupling in Noble Metal Nanostructures. *Chem. Phys. Lett.* **2010**, *487*, 153−164.

(6) Halas, N. J.; Lal, S.; Chang, W.-S.; Link, S.; Nordlander, P. Plasmons in Strongly Coupled Metallic Nanostructures. *Chem. Rev.* **2011**, *111*, 3913−3961.

(7) Klinkova, A.; Choueiri, R. M.; Kumacheva, E. Self-Assembled Plasmonic Nanostructures. *Chem. Soc. Rev.* **2014**, *43*, 3976−3991.

(8) Nie, Z. H.; Petukhova, A.; Kumacheva, E. Properties and Emerging Applications of Self-Assembled Structures Made From Inorganic Nanoparticles. *Nat. Nanotechnol.* **2010**, *5*, 15−25.

(9) Vigderman, L.; Khanal, B. P.; Zubarev, E. R. Functional Gold Nanorods: Synthesis, Self-Assembly, and Sensing Applications. *Adv. Mater.* **2012**, *24*, 4811−4841.

(10) Chen, H.; Shao, L.; Li, Q.; Wang, J. Gold Nanorods and Their Plasmonic Properties. *Chem. Soc. Rev.* **2013**, *42*, 2679−2724.

(11) Ming, T.; Kou, X.; Chen, H.; Wang, T.; Tam, H.-L.; Cheah, K.-W.; Chen, J.-Y.; Wang, J. Ordered Gold Nanostructure Assemblies Formed By Droplet Evaporation. *Angew. Chem., Int. Ed.* **2008**, *47*, 9685−9690.

(12) Giannini, V.; Fernández-Domínguez, A. I.; Heck, S. C.; Maier, S. A. Plasmonic Nanoantennas: Fundamentals and Their Use in Controlling the Radiative Properties of Nanoemitters. *Chem. Rev.* **2011**, *111*, 3888−3912.

(13) Stewart, M. E.; Anderton, C. R.; Thompson, L. B.; Maria, J.; Gray, S. K.; Rogers, J. A.; Nuzzo, R. G. Nanostructured Plasmonic Sensors. *Chem. Rev.* **2008**, *108*, 494−521.

(14) Mubeen, S.; Lee, J.; Singh, N.; Krämer, S.; Stucky, G. D.; Moskovits, M. An Autonomous Photosynthetic Device in Which All Charge Carriers Derive from Surface Plasmons. *Nat. Nanotechnol.* **2013**, *8*, 247−251.

(15) Lee, J.; Mubeen, S.; Ji, X.; Stucky, G. D.; Moskovits, M. Plasmonic Photoanodes for Solar Water Splitting with Visible Light. *Nano Lett.* **2012**, *12*, 5014−5019.

(16) Brongersma, M. L.; Halas, N. J.; Nordlander, P. Plasmon-Induced Hot Carrier Science and Technology. *Nat. Nanotechnol.* **2015**, *10*, 25−34.

(17) Aroca, R. F. Plasmon Enhanced Spectroscopy. *Phys. Chem. Chem. Phys.* **2013**, *15*, 5355−5363.

DOI: 10.1021/acsphotonics.5b00369
ACS Photonics 2015, 2, 1482−1488

(18) Tokel, O.; Inci, F.; Demirci, U. Advances in Plasmonic Technologies for Point of Care Applications. *Chem. Rev.* **2014**, *114*, 5728−5752.
(19) Schlücker, S. Surface-Enhanced Raman Spectroscopy: Concepts and Chemical Applications. *Angew. Chem., Int. Ed.* **2014**, *53*, 4756−4795.
(20) Alvarez-Puebla, R. A.; Liz-Marzán, L. M. SERS Detection of Small Inorganic Molecules and Ions. *Angew. Chem., Int. Ed.* **2012**, *51*, 11214−11223.
(21) Beermann, J.; Novikov, S. M.; Albrektsen, O.; Nielsen, M. G.; Bozhevolnyi, S. I. Surface-enhanced Raman Imaging of Fractal Shaped Periodic Metal Nanostructures. *J. Opt. Soc. Am. B* **2009**, *26*, 2370−2376.
(22) Evlyukhin, A. B.; Kuznetsov, A. I.; Novikov, S. M.; Beermann, J.; Reinhardt, C.; Kiyan, R.; Bozhevolnyi, S. I.; Chichkov, B. N. Optical Properties of Spherical Gold Mesoparticles. *Appl. Phys. B: Lasers Opt.* **2012**, *106*, 841−848.
(23) Zhang, S.-Y.; Regulacio, M. D.; Han, M.-Y. Self-Assembly of Colloidal One-Dimensional Nanocrystals. *Chem. Soc. Rev.* **2014**, *43*, 2301−2323.
(24) Alvarez-Puebla, R. A.; Agarwal, A.; Manna, P.; Khanal, B. P.; Aldeanueva-Potel, P.; Carbó-Argibay, E.; Pazos-Pérez, N.; Vigderman, L.; Zubarev, E. R.; Kotov, N. A.; Liz-Marzán, L. M. Gold Nanorods 3D-Supercrystals as Surface Enhanced Raman Scattering Spectroscopy Substrates for the Rapid Detection of Scrambled Prions. *Proc. Natl. Acad. Sci. U. S. A.* **2011**, *108*, 8157−8161.
(25) Thorkelsson, K.; Bai, P.; Xu, T. Self-Assembly and Applications of Anisotropic Nanomaterials: A review. *Nano Today* **2015**, *10*, 48−66.
(26) Peng, B.; Li, G.; Li, D.; Dodson, S.; Zhang, Q.; Zhang, J.; Lee, Y. H.; Demir, H. V.; Ling, X. Y.; Xiong, Q. Vertically Aligned Gold Nanorod Monolayer on Arbitrary Substrates: Self-Assembly and Femtomolar Detection of Food Contaminants. *ACS Nano* **2013**, *7*, 5993−6000.
(27) Gómez-Graña, S.; Pérez-Juste, J.; Alvarez-Puebla, R. A.; Guerrero-Martínez, A.; Liz-Marzán, L. M. Self-Assembly of Au@Ag Nanorods Mediated by Gemini Surfactants for Highly Efficient SERS-Active Supercrystals. *Adv. Opt. Mater.* **2013**, *1*, 477−481.
(28) Hamon, C.; Novikov, S.; Scarabelli, L.; Basabe-Desmonts, L.; Liz-Marzán, L. M. Hierarchical Self-Assembly of Gold Nanoparticles into Patterned Plasmonic Nanostructures. *ACS Nano* **2014**, *8*, 10694−10703.
(29) Hamon, C.; Postic, M.; Mazari, E.; Bizien, T.; Dupuis, C.; Even-Hernandez, P.; Jimenez, A.; Courbin, L.; Gosse, C.; Artzner, F.; Marchi-Artzner, V. Three-Dimensional Self-Assembling of Gold Nanorods with Controlled Macroscopic Shape and Local Smectic B Order. *ACS Nano* **2012**, *6*, 4137−4146.
(30) Xie, Y.; Guo, S.; Ji, Y.; Guo, C.; Liu, X.; Chen, Z.; Wu, X.; Liu, Q. Self-Assembly of Gold Nanorods into Symmetric Superlattices Directed by OH-Terminated Hexa(ethylene glycol) Alkanethiol. *Langmuir* **2011**, *27*, 11394−11400.
(31) Solís, D. M.; Taboada, J. M.; Obelleiro, F.; Liz-Marzán, L. M.; García de Abajo, F. J. Toward Ultimate Nanoplasmonics Modeling. *ACS Nano* **2014**, *8*, 7559−7570.
(32) Solis, D. M.; Araujo, M. G.; Landesa, L.; Garcia, S.; Taboada, J. M.; Obelleiro, F. MLFMA-MoM For Solving The Scattering of Densely Packed Plasmonic Nanoparticle Assemblies. *IEEE Photonics J.* **2015**, *7*, 1.
(33) Solis, D. M.; Taboada, J. M.; Obelleiro, F. Surface Integral Equation-Method of Moments With Multiregion Basis Functions Applied to Plasmonics. *IEEE Trans. Antennas Propag.* **2015**, *63*, 2141−2152.
(34) Ye, X.; Jin, L.; Caglayan, H.; Chen, J.; Xing, G.; Zheng, C.; Doan-Nguyen, V.; Kang, Y.; Engheta, N.; Kagan, C. R.; Murray, C. B. Improved Size-Tunable Synthesis of Monodisperse Gold Nanorods through the Use of Aromatic Additives. *ACS Nano* **2012**, *6*, 2804−2817.
(35) Scarabelli, L.; Grzelczak, M.; Liz-Marzán, L. M. Tuning Gold Nanorod Synthesis through Prereduction with Salicylic Acid. *Chem. Mater.* **2013**, *25*, 4232−4238.
(36) Singh, A.; Dickinson, C.; Ryan, K. M. Insight into the 3D Architecture and Quasicrystal Symmetry of Multilayer Nanorod Assemblies from Moiré Interference Patterns. *ACS Nano* **2012**, *6*, 3339−3345.
(37) Apte, A.; Bhaskar, P.; Das, R.; Chaturvedi, S.; Poddar, P.; Kulkarni, S. Self-assembled Vertically Aligned Gold Nanorod Superlattices for Ultra-High Sensitive Detection of Molecules. *Nano Res.* **2015**, *8*, 907−919.
(38) Le Ru, E. C.; Blackie, E.; Meyer, M.; Etchegoin, P. G. Surface Enhanced Raman Scattering Enhancement Factors: A Comprehensive Study. *J. Phys. Chem. C* **2007**, *111*, 13794−13803.
(39) Goris, B.; Bals, S.; Van den Broek, W.; Carbó-Argibay, E.; Gómez-Graña, S.; Liz-Marzán, L. M.; Van Tendeloo, G. Atomic-Scale Determination of Surface Facets in Gold Nanorods. *Nat. Mater.* **2012**, *11*, 930−935.

DOI: 10.1021/acsphotonics.5b00369
ACS Photonics 2015, 2, 1482−1488